

Electrokinetics of metal cylindersJ. E. Flores-Mena,¹ Pablo García-Sánchez,² and Antonio Ramos^{2,*}¹*Facultad de Ciencias de la Electrónica, Benemérita Universidad Autónoma de Puebla, Av. San Claudio y 18 Sur, San Manuel, 72570, CU., FCE2 Puebla, Puebla, México*²*Depto. Electrónica y Electromagnetismo, Facultad de Física, Universidad de Sevilla, Avda. Reina Mercedes s/n, 41012, Sevilla, Spain* (Received 16 November 2018; revised manuscript received 11 February 2019; published 11 March 2019)

We study theoretically the rotation induced on an uncharged metal nanocylinder immersed in an electrolyte by AC electric fields. We consider the rotation of the cylinder when subjected to a rotating electric field (electrorotation) and the orientation of the cylinder in an AC field with constant direction (electro-orientation). The cylinder rotation is due to two mechanisms: the electric field interaction with the induced dipole on the particle and the hydrodynamic stress on the particle originated by the induced-charge electro-osmotic (ICEO) flow around the particle. The cylinder rotation induced by the ICEO mechanism can be calculated by using the Lorentz reciprocal theorem, while the rotation due to the induced dipole is calculated from the cylinder polarizability. We employ 3D numerical computations using finite elements for the general case as well as analytical methods for slender cylinders. Both calculations use the thin-double-layer approximation. We compare the results for slender cylinders of both methods showing good agreement. The electro-orientation (EOr) due to dipole torque aligns the axis of slender cylinders with the applied field, but aligns the axis of short cylinders perpendicularly to the field. The EOr due to ICEO torque always aligns the axis of cylinders with the field. The rotation induced by ICEO torque tends to disappear for frequencies of the applied field much greater than the characteristic frequency for charging the double-layer capacitance of the metal-electrolyte interface.

DOI: [10.1103/PhysRevE.99.032603](https://doi.org/10.1103/PhysRevE.99.032603)**I. INTRODUCTION**

Manipulation of small particles in suspension can be achieved by means of AC electric fields [1] and it has been an important topic of research during the past decades in the fields of colloids and biotechnology [2–4]. Recently, electrokinetic manipulation of metal and semiconducting microparticles has been explored in the context of microfluidics and nanoelectronics [5–9]. For example, ac fields are used to assemble Janus spheres and form chains of metallodielectric particles [10,11]. Janus spheres subjected to electric fields are also used as cargo carriers for specific targets [12]. Suspensions of metal nanoparticles subjected to ac fields form microwires between electrodes [13,14]. References [15–17] report the positioning and rotation of metal nanowires. Reference [18] demonstrates frequency-dependent assembly patterns of metal nanowires with ac fields and Ref. [19] shows how to use ac electric fields to separate metal nanowires from semiconducting carbon nanotubes.

An important number of recent works have been focused on the study of the physical mechanisms behind the electrokinetic manipulation of metal microparticles, as reviewed in Ref. [20]. These works demonstrate that the electrokinetic motion of metal particles arises from the interaction of the applied electric fields with the induced charges in the electrical double layer (EDL) at the particle-electrolyte interface. As a consequence of this interaction, two distinct mechanisms appear: The action of the electric field on the induced electric

dipole and the motion that arises from the viscous stresses originated by the induced electro-osmotic (ICEO) flow around the particle [21,22]. The relative importance of these mechanisms is manifested in the following phenomena:

(1) The displacement of a particle suspended in an electrolyte and subjected to a nonuniform field is known as “dipolophoresis” [23–25]. Theoretically, dipolophoresis of metal particles is influenced by the two mechanisms: ICEO flows and forces on the induced dipole. However, recent experiments with gold-coated microspheres subjected to nonuniform fields show that the main mechanism behind their displacement is the action on the induced dipole [26]. In this case, when the motion is driven by the force on the induced dipole, the particle displacement is known as “dielectrophoresis” (DEP).

(2) “Electrorotation” (ROT) is the particle rotation due to a rotating electric field. ROT of metal particles results from the combination of counterfield rotation originated by the action on the induced dipole, and cofield rotation that arises from the ICEO flow around the particle [27]. This cofield rotation vanishes for metal spheres much larger than the Debye screening length of the electrolyte (around 10–100 nm for aqueous electrolytes). Therefore, ROT of metal microspheres is counterfield and driven by the action on the induced dipole, in agreement with experimental results [26,28,29]. However, ROT of metal cylinders is affected by both mechanisms [30] and one goal of the present work is the evaluation of the relative importance between them. For example, approximate analytical solutions for the electrorotation of perfectly polarizable spheroids are found in Ref. [31] and the results therein show that, theoretically, the two mechanisms have the

*ramos@us.es

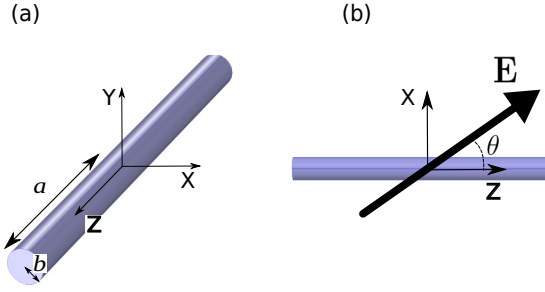


FIG. 1. Metal cylinder subjected to an ac electric field.

same relative influence for prolate spheroids. The study for polarizable spheroids has been recently extended to arbitrary applied electric fields in Ref. [32].

(3) The orientation of a non-spherical particle in an electric field with constant direction is known as “Electro-orientation” (EOr). Several experimental works show that metal nanowires tend to align with the applied electric field [33,34]. For low frequencies, EOr is mainly induced by ICEO flow around the particle [35,36], while at high frequencies the motion is originated by the torque on the induced dipole [33]. Ref. [31] includes solutions for the electro-orientation of polarizable spheroids with arbitrary aspect ratio, but it uses an approximate boundary condition of the EDL charging to obtain analytical solutions. One goal of the present work is to find numerical solutions for EOr of metal nanowires, as used in experiments, using the exact EDL charging boundary condition.

In this work we study theoretically the electrokinetic motion induced in a metal cylinder immersed in an electrolyte. We consider two cases, the rotation of the cylinder when subjected to a rotating electric field and the orientation of the cylinder in an AC field with constant direction. The rotational motion originated by the ICEO mechanism can be calculated by using the Lorentz reciprocal theorem, while the motion due to the induced dipole is calculated from the cylinder polarizability. These calculations are carried out with two different approaches under the thin-double-layer approximation: analytical methods for slender cylinders, and 3D numerical computations using finite elements for the general case. Previous work [33] focused on slender cylinders and presented 2D axisymmetric numerical calculations of the rotation due to dipole and an analytical solution of nanowire rotation due to dipole and ICEO flow. In the present manuscript, we analyze the rotation of finite cylinders due to both mechanisms using 3D numerical calculations and improve the slender-body approximation with an expansion up to second order of the small parameter.

II. THEORY

Let us consider a metal cylinder with radius b and length $2a$ immersed in a 1:1 symmetric electrolyte as, for instance, potassium chloride. The cylinder rests on the ZX plane and its axis is aligned with the Z axis, as shown in Fig. 1(a). The metal cylinder is subjected to an external ac electric field of amplitude E_0 and angular frequency ω , as shown in Fig. 1(b).

In EOr experiments, the electric field is given by

$$\mathbf{E}(t) = E_0 \text{Re}[(\cos \theta \mathbf{u}_z + \sin \theta \mathbf{u}_x) e^{i\omega t}], \quad (1)$$

where $\text{Re}[\dots]$ stands for real part and \mathbf{u}_j for unit vector of j coordinate. In ROT experiments, the electric field is

$$\mathbf{E}(t) = E_0 \text{Re}[(\mathbf{u}_z - i\mathbf{u}_x) e^{i\omega t}], \quad (2)$$

corresponding to an anticlockwise rotating electric field within the ZX plane of Fig. 1(b).

As usual in electrokinetics problems, we assume that the electric potential and the ionic concentrations satisfy the Poisson-Nernst-Planck (PNP) equations [37]. Also, we consider the approximation of small applied electric potential, which in the present problem can be written as $E_0 R \ll k_B T/e$, where R is a typical particle dimension and $k_B T/e$ the thermal voltage (≈ 25 mV at room temperature). The weak-field approximation guarantees that charge convection is negligible and the electrical problem can be solved independently, with its solution then inserted into the mechanical problem [24]. In addition, we assume that the Debye length is much smaller than typical dimensions of the cylinder. This allows us to apply the thin-double-layer approximation, which is usually valid for micron-sized particles. Under these approximations, the electric potential can be written as $\phi(\mathbf{r}, t) = \text{Re}[\Phi(\mathbf{r}) e^{i\omega t}]$, where the potential phasor $\Phi(\mathbf{r})$ satisfies Laplace’s equation in the bulk electrolyte,

$$\nabla^2 \Phi = 0, \quad (3)$$

with boundary condition on the surface of the particle,

$$\sigma \frac{\partial \Phi}{\partial n} = i\omega C_{\text{DL}} (\Phi - V), \quad (4)$$

where σ is the electrolyte conductivity, C_{DL} is the EDL capacitance, V is the potential of the metal particle, and the normal derivative is taken from the particle to the electrolyte. From symmetry we will take $V = 0$ in our case. An estimate of the EDL capacitance is given by $C_{\text{DL}} = \varepsilon/\lambda_D$, where ε is the liquid permittivity and λ_D , the Debye length. The boundary condition expresses the charge conservation on a perfectly polarizable surface: the current arriving from the bulk charges the EDL capacitor. Therefore, we have assumed that the voltage across the EDL is below the threshold voltage to induce Faradaic reactions. We have also assumed that the frequency is small enough $\omega \ll \sigma/\varepsilon$ to consider the diffuse layer is in quasiequilibrium [38].

With respect to the mechanical problem, the Reynolds number is small enough so that the fluid velocity \mathbf{v} and pressure p satisfy Stokes and continuity equations

$$\eta \nabla^2 \mathbf{v} = \nabla p, \quad \nabla \cdot \mathbf{v} = 0, \quad (5)$$

where η is the liquid dynamic viscosity. The boundary condition on (b.c.) the surface of the particle is written as

$$\mathbf{v} = \mathbf{v}_s + \mathbf{U} + \boldsymbol{\Omega} \times \mathbf{r}, \quad (6)$$

where \mathbf{U} is the velocity of the particle center of reaction, $\boldsymbol{\Omega}$ is the particle angular velocity, \mathbf{r} is the displacement from the reaction center to a point on the particle surface, and \mathbf{v}_s is the Helmholtz-Smoluchowski slip velocity. The latter is given by $\mathbf{v}_s = -(\varepsilon/\eta)\zeta \mathbf{E}_s$ for a thin double layer in quasi-equilibrium on a perfectly polarizable metal surface [39]. Here ζ is the

zeta potential i.e., the potential drop in the diffuse layer, and \mathbf{E}_s is the tangential electric field just outside the EDL. We are interested in the time-averaged velocity, which can be written using phasors as [20]

$$\mathbf{v}_s = -\frac{\varepsilon\Lambda}{4\eta}\nabla_s|\Phi - V|^2, \quad (7)$$

where ∇_s is the tangential gradient operator, and Λ is a parameter that relates the induced ζ potential to the total EDL voltage $\Phi - V$. In the ideal case, $\zeta = V - \Phi$ and $\Lambda = 1$. Experimental observations show that $\Lambda < 1$ and sometimes very much smaller [40].

Since particle inertia is negligible, the balance of forces and torques determines the translational velocity \mathbf{U} and the angular velocity $\boldsymbol{\Omega}$. It is convenient to describe the velocity field as the result of two distinct contributions: the flow generated by a translating and rotating particle and the flow generated by the slip velocity on a stationary particle. In this way, the equilibrium of forces and torques for cylinders can be written as

$$\eta\mathbb{M} \cdot \mathbf{U} = \langle (\mathbf{p} \cdot \nabla)\mathbf{E} \rangle + \int_{S_p} \mathbb{T}_H \cdot d\mathbf{S}, \quad (8)$$

$$\eta\mathbb{N} \cdot \boldsymbol{\Omega} = \langle \mathbf{p} \times \mathbf{E} \rangle + \int_{S_p} \mathbf{r} \times \mathbb{T}_H \cdot d\mathbf{S}, \quad (9)$$

where $\langle \dots \rangle$ stands for time average, \mathbb{T}_H is the hydrodynamic stress tensor for the velocity field originated by the slip velocity on a stationary particle, S_p is a surface that encloses the particle with its double layer, and \mathbb{M} and \mathbb{N} are, respectively, the translation and rotation tensors [41]. Notice that for cylinders there is no coupling between translation and rotation since they are orthotropic bodies [41]. In our case, the spatially homogeneous electric fields given by Eqs. (1) and (2) do not produce a translational velocity for cylinders. The angular velocity can be written as $\boldsymbol{\Omega} = \boldsymbol{\Omega}_{\text{DEP}} + \boldsymbol{\Omega}_{\text{ICEP}}$, with

$$\begin{aligned} \boldsymbol{\Omega}_{\text{DEP}} &= \eta^{-1}\mathbb{N}^{-1} \cdot \langle \mathbf{p} \times \mathbf{E} \rangle, \\ \boldsymbol{\Omega}_{\text{ICEP}} &= \eta^{-1}\mathbb{N}^{-1} \cdot \int_{S_p} \mathbf{r} \times \mathbb{T}_H \cdot d\mathbf{S}, \end{aligned} \quad (10)$$

where the subscripts DEP and ICEP refer, respectively, to particle rotation due to torque on the induced dipole or due to ICEO flow around the particle.

A. Angular velocity due to induced dipole

Using phasors, the dipole induced on the cylinder can be written as $\mathbf{p} = \alpha_z\mathbf{E}_z + \alpha_x\mathbf{E}_x$, where \mathbf{E}_z and \mathbf{E}_x are, respectively, the applied electric field components parallel and perpendicular to the cylinder axis, and α_z and α_x are the corresponding polarizabilities. The time-averaged DEP torque is then given by

$$\boldsymbol{\tau}_e = \frac{1}{2}\text{Re}[\mathbf{p} \times \mathbf{E}^*] = \frac{1}{2}\text{Re}[\alpha_z E_z E_x^* - \alpha_x E_x E_z^*]\mathbf{u}_y, \quad (11)$$

where asterisk (*) stands for complex conjugate. For the EO case,

$$\boldsymbol{\tau}_e = \frac{1}{2}\text{Re}[\alpha_z - \alpha_x]E_0^2 \cos\theta \sin\theta \mathbf{u}_y, \quad (12)$$

and for the ROT case,

$$\boldsymbol{\tau}_e = -\frac{1}{2}\text{Im}[\alpha_z + \alpha_x]E_0^2 \mathbf{u}_y, \quad (13)$$

where $\text{Im}[\dots]$ means imaginary part.

We obtain $\boldsymbol{\Omega}_{\text{DEP}}$ dividing the electrical torque by the rotational viscous friction coefficient around Y axis.

B. Angular velocity due to ICEO flow

We will show in this section that $\boldsymbol{\Omega}_{\text{ICEP}}$ can be expressed as a certain surface integral of the slip velocity v_s on the particle surface thanks to the Lorentz reciprocal theorem [42].

As mentioned above, the fluid velocity on the particle surface Eq. (6) can be decomposed as the sum of two flows which are solutions of the Stokes equations: the flow induced by the slip velocity on the stationary cylinder (problem 1) and the flow generated by a translating and rotating particle (problem 2). Let \mathbb{T}_1 and \mathbb{T}_2 be, respectively, the hydrodynamic stress tensors that arise from the solutions of these two problems. Application of the Lorentz reciprocal theorem [41,43] results in

$$\int \mathbf{n} \cdot [\mathbb{T}_1 \cdot (\mathbf{U} + \boldsymbol{\Omega} \times \mathbf{r})] dS = \int \mathbf{n} \cdot (\mathbb{T}_2 \cdot \mathbf{v}_s) dS, \quad (14)$$

where the integrations are performed over the particle surface and \mathbf{n} is a unit vector normal to the particle.

In the present case we are interested in the particle rotation induced by the ICEO slip velocity on the cylinder surface originated by the homogeneous fields of Eqs. (1) and (2). Therefore, we choose $\mathbf{U} = 0$ and $\boldsymbol{\Omega} = \boldsymbol{\Omega}_{\text{ICEP}}\mathbf{u}_y$. Since this is a torque-free problem, $\int \mathbf{r} \times (\mathbf{n} \cdot \mathbb{T}_1) dS = -\int \mathbf{r} \times (\mathbf{n} \cdot \mathbb{T}_2) dS$, and Eq. (14) can be transformed into

$$-\int \mathbf{r} \times (\mathbf{n} \cdot \mathbb{T}_2) dS \cdot \boldsymbol{\Omega}_{\text{ICEP}}\mathbf{u}_y = \int \mathbf{n} \cdot (\mathbb{T}_2 \cdot \mathbf{v}_s) dS. \quad (15)$$

And solving for $\boldsymbol{\Omega}_{\text{ICEP}}$,

$$\boldsymbol{\Omega}_{\text{ICEP}} = \frac{\int \mathbf{n} \cdot (\mathbb{T}_2 \cdot \mathbf{v}_s) dS}{\int (x(\mathbf{n} \cdot \mathbb{T}_2)_z - z(\mathbf{n} \cdot \mathbb{T}_2)_x) dS}. \quad (16)$$

Up to here \mathbb{T}_2 is the hydrodynamic stress tensor corresponding to the cylinder rotating with angular velocity $\boldsymbol{\Omega}_{\text{ICEP}}$. However, since the fluid equations are linear, we can now choose \mathbb{T}_2 to be the one corresponding to a rotating cylinder with $\boldsymbol{\Omega} = 1$. According to Eq. (16), the rotation velocity generated by the ICEO flow can be calculated from the solution of the slip electro-osmotic velocity on the particle and the hydrodynamic stress tensor generated by a rotating cylinder. Therefore, thanks to the reciprocal theorem, we avoid to solve the liquid velocity field that arises from the electro-osmotic velocity. Note that the denominator in Eq. (16) corresponds to the viscous friction coefficient around Y axis.

III. MATHEMATICAL METHODS

The rotational particle motion given by previous equations is obtained by using analytical methods in the case of slender cylinders [33,35,36] and 3D numerical calculations in the general case. In both methods it will be convenient to consider the total electrical potential as the sum of the potentials Φ_a and Φ_b corresponding, respectively, to the potentials generated by the applied electric field along the cylinder axis $\mathbf{E}_a = E_{0a}e^{i\omega t}\mathbf{u}_z$ and perpendicular to the axis $\mathbf{E}_b = E_{0b}e^{i\omega t}\mathbf{u}_x$ (see Fig. 1).

A. Slender particle approximation

The results presented in this section are an improvement of previous analytical expressions [33] since the induced linear charge is expanded up to second order.

1. Electrical potentials Φ_a and Φ_b

The applied electric field along the axial direction ($\mathbf{E}_a = E_{0a}e^{i\omega t}\mathbf{u}_z$) induces a distribution of charges on the cylinder. Using slender-body approximation, the electric potential outside the cylinder can be written in cylindrical coordinates (ρ, z) as the sum of the applied electric potential plus the potential created by an effective linear charge density $\lambda(z)$ along the Z axis [44–46]:

$$\Phi_a = -E_{0a}z + \frac{1}{4\pi\epsilon} \int_{-a}^a \frac{\lambda(z')}{\sqrt{(z-z')^2 + \rho^2}} dz'. \quad (17)$$

We imagine that the nanowires are cylinders with rounded ends with $a \gg b$, so that we can apply this slender-body approximation. The boundary condition Eq. (4) at the cylinder surface, $\rho = b$, is

$$i\omega C_{DL} \Phi_a|_{\rho=b} = \sigma \left. \frac{\partial \Phi_a}{\partial \rho} \right|_{\rho=b}. \quad (18)$$

Substitution of Eq. (17) into Eq. (18) leads to an integral equation for $\lambda(z)$, which can be solved numerically [47]. Here we proceed analytically by doing an expansion of the linear charge [46] in powers of the small parameter $1/\ln(a/b)$ ($a/b \gg 1$),

$$\lambda(z) \sim \frac{\lambda_1(z)}{\ln(a/b)} + \frac{\lambda_2(z)}{[\ln(a/b)]^2} + \frac{\lambda_3(z)}{[\ln(a/b)]^3} + \dots, \quad (19)$$

and the integrals are approximated asymptotically. We expand $\lambda(z)$ up to second order in this work. The details are provided in Appendix A. The induced dipole p_z and the potential on the cylinder surface are, respectively,

$$p_z = \int_{-a}^a z\lambda(z)dz = \frac{4\pi\epsilon a^3 E_{0a}}{3\ln(a/b)} \Xi \left[1 + \frac{0.947039}{\ln(a/b)} \Xi \right], \quad (20)$$

$$\begin{aligned} \Phi_a(b, z) &= -\frac{E_{0a}z}{1 + i\tilde{\omega}_b \ln(a/b)} \left\{ 1 + \frac{1 - \ln[2\sqrt{1 - (z/a)^2}]}{\ln(a/b)} \Xi \right\}, \\ &\quad (21) \end{aligned}$$

where $\Xi = i\tilde{\omega}_b \ln(a/b)/[1 + i\tilde{\omega}_b \ln(a/b)]$ and $\tilde{\omega}_b = \omega C_{DL} b/\sigma$ is a nondimensional frequency.

For $\tilde{\omega}_b \gg 1/\ln(a/b)$, $\Phi_a(b, z)$ tends to zero so that the cylinder is equipotential and behaves as a perfect conductor. For $\tilde{\omega}_b \ll 1/\ln(a/b)$, $\Phi_a(b, z)$ tends to $-E_{0a}z$, i.e., the applied potential, and the cylinder behaves as a perfect insulator with the polarizability going to 0. The characteristic frequency given by the slender-body approximation is in dimensional form $\omega_{RC} = \sigma/bC_{DL} \ln(a/b)$, while the order of magnitude for the polarizability is $|\alpha_z| \sim 4\pi\epsilon a^3/3\ln(a/b)$ [33].

The electrical potential Φ_b is generated by the applied electric field $\mathbf{E}_b = E_{0b}e^{i\omega t}\mathbf{u}_x$. Neglecting edge effects, the electric potential near the slender cylinder, that satisfies the b.c. $i\omega C_{DL} \Phi_b = \sigma(\partial \Phi_b/\partial \rho)$ at $\rho = b$, is written in polar

coordinates (ρ, ϕ) as [33]

$$\Phi_b = -E_{0b}\rho \cos \phi + \left(\frac{i\tilde{\omega}_b - 1}{i\tilde{\omega}_b + 1} \right) \frac{E_{0b}b^2 \cos \phi}{\rho}. \quad (22)$$

From this expression the induced dipole perpendicular to the cylinder axis is [33]

$$p_x = 4\pi\epsilon E_{0b}ab^2 \frac{i\tilde{\omega}_b - 1}{i\tilde{\omega}_b + 1}. \quad (23)$$

This dipole p_x is of the order of $(b/a)^2 \ln(a/b)$ smaller than p_z .

2. Induced rotations

The time-averaged torque on the induced dipole [Eq. (11)] in the slender approximation is $\tau_e = \frac{1}{2} \text{Re}[\alpha_z E_z E_x^*] \mathbf{u}_y$, where

$$\alpha_z = \frac{4\pi\epsilon a^3}{3\ln(a/b)} \Xi \left[1 + \frac{0.947039}{\ln(a/b)} \Xi \right], \quad (24)$$

and the torque on \mathbf{p}_x has been neglected because α_x is of the order of $(b/a)^2 \alpha_z$.

The EOR torque is obtained when $E_{0a} = E_0 \cos \theta$ and $E_{0b} = E_0 \sin \theta$ [Eq. (12)] $\tau_e = \frac{1}{2} \text{Re}[\alpha_z] E_0^2 \cos \theta \sin \theta \mathbf{u}_y$. This torque tends to align the cylindrical particle with the applied field. The ROT torque is obtained when $E_{0a} = E_0$ and $E_{0b} = -iE_0$ [Eq. (13)] $\tau_e = -\frac{1}{2} \text{Im}[\alpha_z] E_0^2 \mathbf{u}_y$. The ROT torque is negative, which means that the particle rotates in the opposite direction to the rotating applied field (counterfield rotation).

The angular velocity due to this electrical torque on the induced dipole is obtained from the balance with the viscous friction $\gamma \Omega = \tau_e$. The viscous coefficient γ for a slender cylinder up to the same order of approximation is [48,49]

$$\gamma = \frac{8\pi\eta a^3}{3\ln(a/b)} \left[1 + \frac{11/6 - \ln 4}{\ln(a/b)} \right], \quad (25)$$

so that the electrically induced angular velocity is

$$\begin{aligned} \Omega_{DEP} &= \frac{\epsilon}{4\eta} \left[1 + \frac{0.447039}{\ln(a/b)} \right]^{-1} \\ &\quad \times \text{Re} \left\{ \Xi \left[1 + \frac{0.947039}{\ln(a/b)} \Xi \right] E_{0a} E_{0b}^* \right\}. \end{aligned} \quad (26)$$

The rotation due to the induced charge electro-osmotic flow around the cylinder is obtained from the expressions of Φ_a [Eq. (21)] and Φ_b [Eq. (22)] on the cylinder surface. The time-averaged electro-osmotic slip velocity on the surface of the particle is proportional to $(\Phi_a + \Phi_b) \nabla_s (\Phi_a + \Phi_b)^*$ [Eq. (7)]. The terms $\Phi_a \nabla_s \Phi_a^*$ and $\Phi_b \nabla_s \Phi_b^*$ do not generate rotation because of symmetry. For a slender body only the contribution of $\Phi_a \nabla_s \Phi_b^*$ is required [33,36,50]. Therefore, the rotation is due to the slip velocity generated by the induced ζ potential due to the field along the axis actuated by the field perpendicular to the axis. The slip velocity proportional to this term is

$$\mathbf{v}_s^{\text{rot}} = -(\epsilon\Lambda/2\eta) \text{Re} \left[\frac{2E_{0b}^* \Phi_a}{1 - i\tilde{\omega}_b} \right] \sin \phi \mathbf{u}_\phi. \quad (27)$$

Using the reciprocal theorem and the slender-body approximation, Solomentsev and Anderson [50] provided the

following angular velocity expression for cylinders

$$\Omega_{\text{ICEP}} = -\frac{\int_{-1}^1 f(s)\tilde{v}(s)ds}{\int_{-1}^1 sf(s)ds}, \quad (28)$$

where $s = z/a$,

$$f(s) = \frac{s(2\ln(a/b) + 1 - 2\ln(2\sqrt{1-s^2}))}{4[\ln(a/b)]^2}, \quad (29)$$

and \tilde{v}_s is obtained by averaging $\mathbf{u}_x \cdot \mathbf{v}_s^{\text{rot}}$ over ϕ ,

$$\tilde{v}_s = -(\varepsilon\Lambda/2\eta)\text{Re}\left[\frac{2E_{0b}^*\Phi_a}{1-i\tilde{\omega}_b}\right]. \quad (30)$$

The result is

$$\begin{aligned} \Omega_{\text{ICEP}} &= \frac{\varepsilon\Lambda}{2\eta}\text{Re}\left\{\frac{E_{0a}E_{0b}^*}{(1-i\tilde{\omega}_b)[1+i\tilde{\omega}_b\ln(a/b)]}\left[1+\frac{0.947039}{\ln(a/b)}\Xi\right]\right\}. \end{aligned} \quad (31)$$

For electro-orientation ($E_{0a} = E_0 \cos \theta$ and $E_{0b} = E_0 \sin \theta$) the angular velocity is positive and the particle tends to align with the field. For electrorotation ($E_{0a} = E_0$ and $E_{0b} = -iE_0$) the angular velocity results in positive values and the particle rotates in the same direction of rotation as the electric field (cofield rotation).

B. Finite elements

The computation of the EOr and ROT of nonslender cylinders requires of 3D numerical simulations. The electrical and mechanical problems were solved using the commercial finite element solver COMSOL. The electrical potentials Φ_a and Φ_b satisfy Eq. (3) with b.c. on the particle surface given by Eq. (4) and with b.c. on outer surface far from the particle $\Phi_a = -z$ and $\Phi_b = -x$, respectively. The fluid velocity and pressure generated by a rotating cylinder around Y axis satisfy Eqs. (5) with b.c. on the particle surface $\mathbf{v} = \mathbf{u}_y \times \mathbf{r}$ and with no slip b.c. on outer surface far from the particle.

Once the potentials Φ_a and Φ_b are obtained, the polarizabilities α_z and α_x are calculated by taking into account that the dipole moment of a charge distribution is equal to the following integration on a spherical surface that encloses the charges [51]

$$\mathbf{p} = 3\varepsilon \oint \Phi'(\mathbf{r})d\mathbf{S}\mathbf{n}, \quad (32)$$

where Φ' is the potential generated by the charge distribution, which is the perturbation to the applied potential $\Phi' = \Phi + \mathbf{E}_0 \cdot \mathbf{r}$. The angular velocity Ω_{DEP} is obtained dividing the electrical torque by the viscous friction coefficient γ computed in the hydrodynamic problem.

The angular velocity due to ICEO is obtained by the surface integration of \mathbf{v}_s given in Eq. (16), with the hydrodynamic stress tensor \mathbb{T}_2 of the rotating cylinder around Y axis. The slip velocity is proportional to $\nabla_s(\Phi_a\Phi_a^* + \Phi_a\Phi_b^* + \Phi_b\Phi_a^* + \Phi_b\Phi_b^*)$, but only the crossed terms produce rotation. In EOr, $\Phi_a = aE_0 \cos \theta \tilde{\Phi}_a$, $\Phi_b = aE_0 \sin \theta \tilde{\Phi}_b$, so that $\nabla_s(\Phi_a\Phi_b^* + \Phi_b\Phi_a^*) = 2E_0^2 \cos \theta \sin \theta \nabla_s \text{Re}[\tilde{\Phi}_a\tilde{\Phi}_b^*]$. While in ROT, $\Phi_a = aE_0\tilde{\Phi}_a$, $\Phi_b = -iaE_0\tilde{\Phi}_b$, so that $\nabla_s(\Phi_a\Phi_b^* +$

$\Phi_b\Phi_a^*) = -2E_0^2 \nabla_s \text{Im}[\tilde{\Phi}_a\tilde{\Phi}_b^*]$. Therefore, $\nabla_s(\tilde{\Phi}_a\tilde{\Phi}_b^*)$ is inserted into Eq. (16), and the real part provides the EOr angular velocity while the imaginary part the ROT angular velocity.

For each cylinder case a convergence test was performed. The 3D discretization was chosen with the compromise of small numerical error and reasonable computational time. To reduce the computational effort, the symmetries of the electrical and hydrodynamic problems were employed so that the domain of computation was reduced to an octant. Details are given in Appendix B. The error committed by the 3D calculations of the polarizability was estimated by comparison with the results of the 2D axisymmetric problem of the axial polarizability. The latter is a 2D numerical calculation so that the axial polarizability can be obtained with high precision by increasing the number of elements with still small computational time. Thus we have an estimate of the error committed by the 3D mesh in the electrical problem. The polarizability α_z was obtained with an error smaller than 0.5% for the different values of $\beta \equiv b/a$ studied. The estimate of the error committed in the hydrodynamic problem is done from comparison with the rotational viscous coefficient [the denominator in Eq. (16)] given in the literature for slender cylinders [52]. The rotational viscous coefficient γ was obtained within 0.5% difference with that given in Ref. [52] for $\beta = 0.04$.

IV. RESULTS

The results are presented in nondimensional form. The nondimensional polarizabilities are defined as $A = \alpha_z/(4\pi\varepsilon a^3)$ and $B = \alpha_x/(4\pi\varepsilon a^3)$. The nondimensional signal frequency is defined as $\tilde{\omega} = \omega C_{\text{DL}}a/\sigma$, which is different to previous nondimensional frequency $\tilde{\omega}_b = \tilde{\omega}b/a$. The nondimensional angular velocity is defined as $\tilde{\Omega} = \eta\Omega/(\varepsilon E_0 E_{0x})$, so that for EOr it is $\tilde{\Omega} = \eta\Omega/(\varepsilon E_0^2 \cos \theta \sin \theta)$ and for ROT it is $\tilde{\Omega} = \eta\Omega/(\varepsilon E_0^2)$. The nondimensional viscous coefficient is $\tilde{\gamma} = \gamma/\eta a^3$. For the DEP cases, the nondimensional angular velocities are

$$\tilde{\Omega}_{\text{EOr}} = \frac{2\pi}{\tilde{\gamma}}\text{Re}[A - B], \quad \tilde{\Omega}_{\text{ROT}} = -\frac{2\pi}{\tilde{\gamma}}\text{Im}[A + B]. \quad (33)$$

Appendix C provides the numerical values of $\tilde{\gamma}$ computed in this work for the different cases analyzed.

The results for slender cylinders are calculated for $\beta \equiv b/a = 0.04$, which was the nanorod slenderness in previous experiments [30,33,34]. The other cases, with greater β , are only obtained numerically. Figure 2 presents the comparison between the polarizabilities calculated numerically and analytically for $\beta = 0.04$ as functions of the nondimensional frequency $\tilde{\omega} = \omega C_{\text{DL}}a/\sigma$. We can see that numerical and analytical values of B , the polarizability perpendicular to the axis, are very close. However, the polarizability along the long axis A presents a greater discrepancy between analytical approximation and numerical results (difference less than 14%). This difference should be ascribed to the fact that in the analytical approximation of A the small parameter is $1/\ln(a/b)$ rather than b/a , so the approximation converges slowly.

Figure 3 shows the imaginary part of the polarizabilities as a function of nondimensional frequency $\tilde{\omega} = \omega C_{\text{DL}}a/\sigma$ for two cases $\beta \equiv b/a = 0.5$ and $\beta = 0.04$. The ROT angular

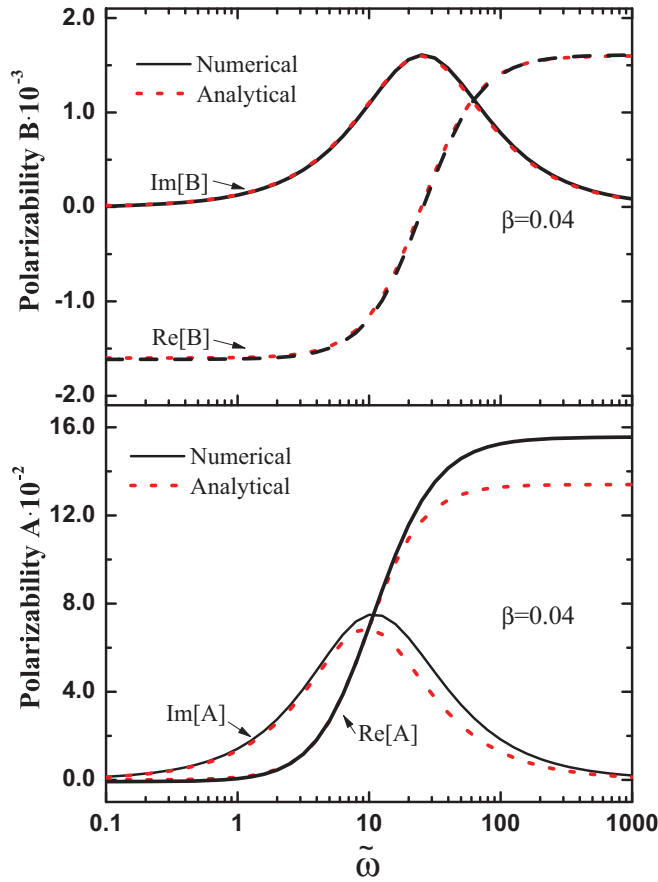


FIG. 2. Comparison between analytical and numerical polarizabilities for $\beta = 0.04$. Polarizabilities A and B as a function of nondimensional frequency $\tilde{\omega} = \omega C_{DL}a/\sigma$.

velocity due to the torque on the dipole is proportional to the imaginary part of $-(A + B)$. The sign of rotation is negative meaning that the rotation is in opposite direction to the electric field rotation, i.e., counterfield rotation. We can see that for a slender cylinder of $\beta = 0.04$ the ROT angular velocity is given mainly by $\text{Im}[A]$, the polarizability along the long axis.

Figure 4 shows the real part of the polarizabilities as a function of nondimensional frequency for two cases $\beta = 0.5$ and $\beta = 0.04$. The real part of $A - B$ is proportional to the EOr angular velocity due to the torque on the dipole. The sign is positive meaning that the torque tends to align the cylinder axis with the field. We can see that for $\beta = 0.04$ the EOr angular velocity is given mainly by $\text{Re}(A)$ for $\tilde{\omega} > 10$, the polarizability along the long axis. At low frequencies, though, $\text{Re}(A)$ is very small and negative but the EOr angular velocity is positive due to the contribution of the dipole perpendicular to the axis.

Figure 5 presents EOr and ROT angular velocities due to dipole torque as functions of nondimensional frequency for a cylinder with $\beta = 1$ (diameter equal to height), and a cube with the same height than the cylinder (edge equal to 2). EOr and ROT velocities are proportional to $\text{Re}[A - B]$ and $-\text{Im}[A + B]$, respectively. The cube cannot rotate in EOr since $A = B$ but it can rotate in ROT. Cylinders with aspect

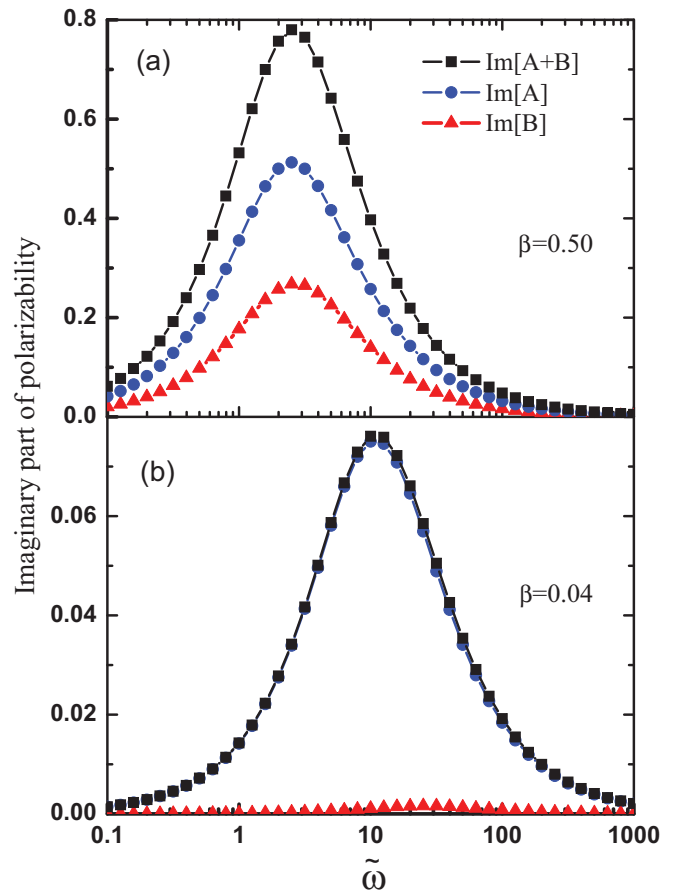


FIG. 3. Imaginary part of polarizabilities as a function of nondimensional frequency $\tilde{\omega} = \omega C_{DL}a/\sigma$ for slenderness $\beta = 0.5$ (a) and $\beta = 0.04$ (b). Also plotted is $\text{Im}[A + B]$ proportional to the angular velocity of rotation in ROT.

ratio close to unity show small EOr rotation and their ROT angular velocity is counter-field.

Figure 6 depicts the nondimensional ICEP angular velocities in EOr and ROT for cylinders with $\beta = 0.04, 0.5, 1$ and a cube as functions of frequency. The value of Λ is equal to one. In all cases, Ω_{ICEP} in EOr shows two limiting values: orientation with the applied field at low frequencies and negligible orientation at high frequencies. With respect to Ω_{ICEP} in ROT, it happens at intermediate frequencies, around the relaxation frequency, and it is several times smaller than Ω_{ICEP} in EOr. The function shows a single maximum for slender cylinders, $\beta = 0.04$, which represents cofield rotation. As can be seen, the angular ICEP velocity from $\beta = 1$ to $\beta = 0.04$ increases as β decreases, i.e., it is greater for slender objects. Figure 6 a shows EOr and ROT angular velocities due to ICEO flow Ω_{ICEP} as functions of $\tilde{\omega}$ for $\beta = 1$ and for a cube with semiedge equal to 1. The angular velocity in ROT is mainly negative for $\beta = 1$, which corresponds to counter-field rotation. For the cube and because of symmetry, Ω_{ICEP} is zero, both for EOr and ROT cases. In this respect, it is similar to the case of a metal sphere that has also Ω_{ICEP} equal to zero for both the EOr and ROT cases [20]. Figure 6(b) plots Ω_{ICEP} versus $\tilde{\omega}$ for $\beta = 0.5$. It can be seen that Ω_{ICEP} for EOr case is much greater than for ROT case. Figure 6(c) compares

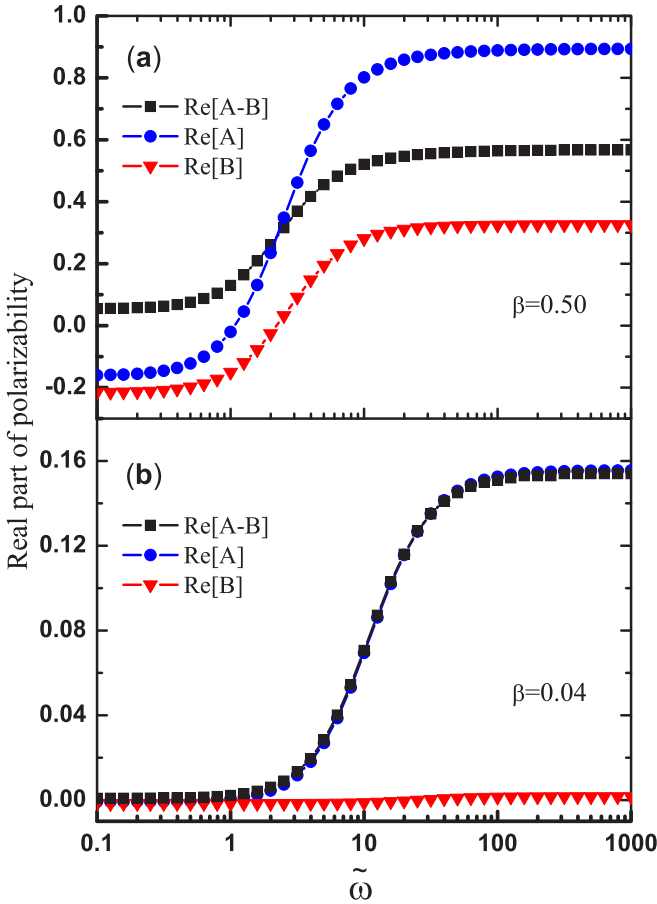


FIG. 4. Real part of polarizabilities as a function of nondimensional frequency $\tilde{\omega} = \omega C_{DL} a / \sigma$ for slenderness $\beta = 0.5$ (a) and $\beta = 0.04$ (b). Also plotted is $\text{Re}[A - B]$ proportional to the angular velocity of rotation in EOr.

numerical and analytical results for Ω_{ICEP} versus $\tilde{\omega}$ for $\beta = 0.04$. The results present a good agreement (difference less than 3.6%). The agreement is better than for the corresponding comparison of Ω_{DEP} and $\beta = 0.04$. We ascribe this to the fact that the ICEP angular velocity is relevant at low frequencies where the numerical solution of the electric potential is close to the analytical solution: The potential is close to the applied potential.

Figure 7 plots the angular velocities due to ICEO flow around the particle ($\Lambda = 1$) and to the torque on the dipole for $\beta = 0.04$. For EOr the angular velocities have the same sign and, therefore, the rod tends to align with the applied electric field at all frequencies. For ROT, the angular velocities go in opposite directions: the ROT due to dipole is counter-field while that due to ICEO flow is cofield. For the comparison with the experiments, the total angular velocity is written as $\Omega = \Omega_{DEP} + \Lambda \Omega_{ICEP}$, where in experiments the parameter Λ is smaller than one [20,33]. We can estimate the value of Λ in the experiments of Ref. [33] by comparison with the present calculations. The ratio between Ω in EOr at low frequency (which is given by the ICEO torque) and Ω in EOr at high frequency (which is given by the dipole torque) is calculated numerically and compared with the same ratio from the experimental results, i.e., $\Delta r_{num} = r_{exp}$, with r the ratio

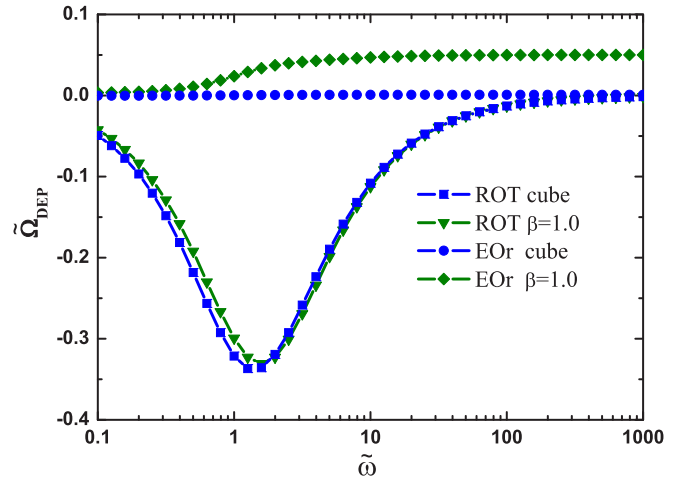


FIG. 5. EOr and ROT angular velocities due to dipole torque for a cylinder with $\beta = 1$ and a cube as functions of nondimensional frequency $\tilde{\omega}$.

between ICEP and DEP angular velocities. The comparison provides an estimated value of $\Lambda \approx 0.1$ for $\sigma = 5$ mS/m. Notice that in the experiments the nanowires, because of their mass density, are close to the bottom of the device exhibiting Brownian motion. Therefore, we have assumed that the nanowire interaction with the bottom wall is the same for

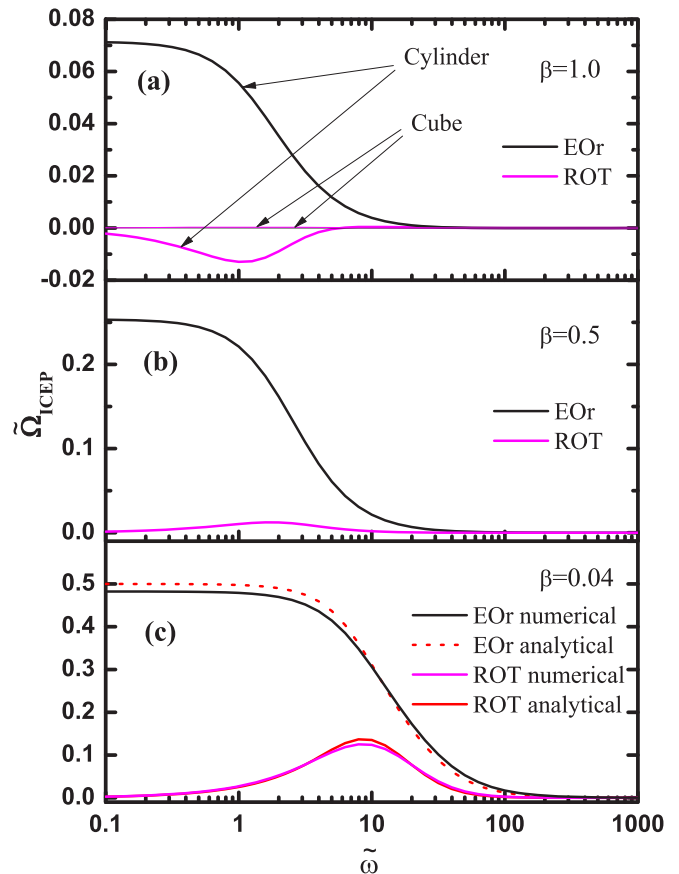


FIG. 6. Angular velocity due to ICEO flow as a function of frequency for cylinders with $b/a = 0.04, 0.5, 1.0$ and a cube.

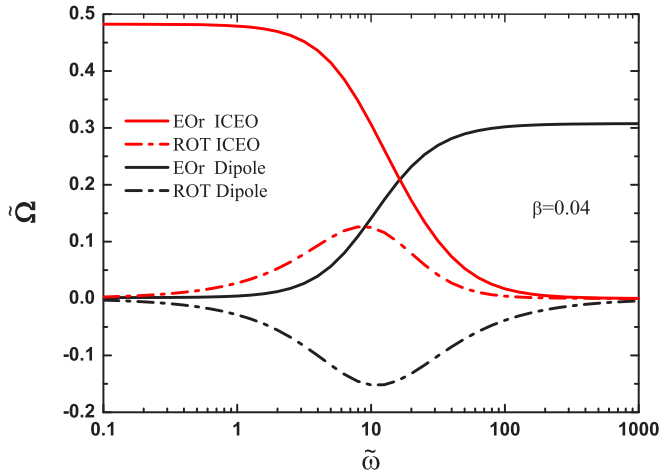


FIG. 7. Angular velocities due to dipole torque, $\tilde{\Omega}_{DEP}$, and to ICEO around the nanowire, $\tilde{\Omega}_{ICEP}$, as a function of frequency for $\beta = 0.04$.

low and high frequencies and can be factored out. To provide some actual numbers, the characteristic frequency given by the maximum rotation in ROT is $\tilde{\omega} \approx 10$. This leads to a signal frequency $f = 10\sigma / (2\pi C_{DL}a) = 38$ kHz, for KCl in water with conductivity $\sigma = 5$ mS/m, nanowire semilength $a = 5$ μ m, and estimating the double layer capacitance by Debye-Huckel expression $C_{DL} = \varepsilon / \lambda_D$. The maximum nondimensional angular velocity in dipole torque ROT is $\tilde{\Omega} \approx 0.15$. This leads to $\Omega = 0.15\varepsilon E_0^2 / \eta = 10.5$ rad/s for a rotating electric field with amplitude $E_0 = 10^4$ V/m.

Figure 8 presents the real part of polarizabilities as a function of frequency for a cylinder with $\beta = 4.0$. It has a diameter four times greater than its height so that the cylinder resembles a disk rather than a rod. Also plotted is $\text{Re}[A - B]$, which is proportional to the angular velocity of rotation in EOr. It is negative for all frequencies which means that the cylinder orients with its symmetry axis perpendicular to the applied

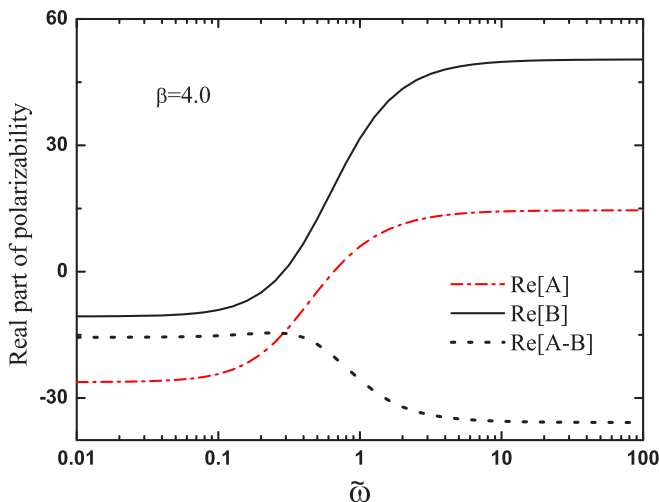


FIG. 8. Real part of polarizabilities A and B as a function of frequency for $\beta = 4.0$. Also plotted is $\text{Re}[A - B]$, which is proportional to the EOr angular velocity.

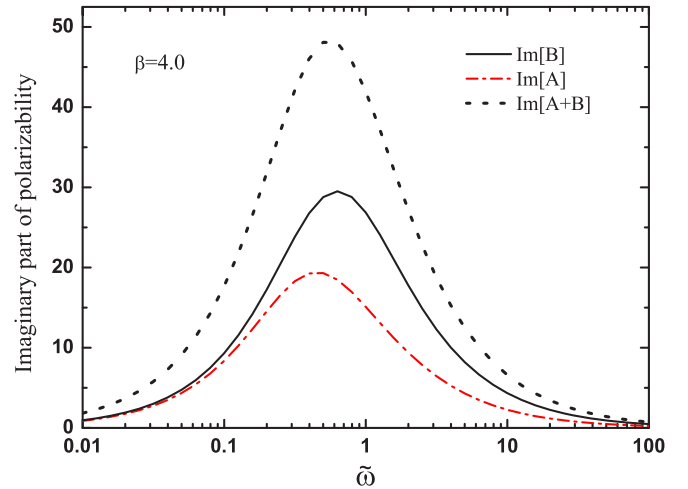


FIG. 9. Imaginary part of polarizabilities A and B as a function of frequency for $\beta = 4.0$. Also plotted is $\text{Im}[A + B]$, which is proportional to the ROT angular velocity.

field. Figure 9 plots the imaginary part of polarizabilities as a function of frequency for a cylinder with $\beta = 4.0$. Also plotted is $\text{Im}[A + B]$, which is proportional to the angular velocity in ROT. In this case, the cylinder rotates counterfield.

Figure 10 shows angular velocities due to dipole torque and to ICEO flow around the particle ($\Lambda = 1$) as a function of frequency for a cylinder with $\beta = 4.0$, i.e., diameter equal to four times height. The EOr torque due to ICEO flow tends to align the cylinder symmetry axis with the applied electric field, $\Omega_{ICEP} > 0$. Interestingly, the EOr torque due to dipole tends to align the cylinder symmetry axis perpendicular to the applied field, $\Omega_{DEP} < 0$. Therefore, if the Λ -factor is not too small ($\Lambda > 0.25$), it would be possible to observe a change in orientation by changing the frequency. With respect to the ROT, Ω_{DEP} is counterfield while Ω_{ICEP} is very small and changes from counterfield to cofield increasing frequency. To give some actual values, the signal frequency for maximum rotation in ROT due to dipole is $f = 0.6\sigma / (2\pi C_{DL}a) =$

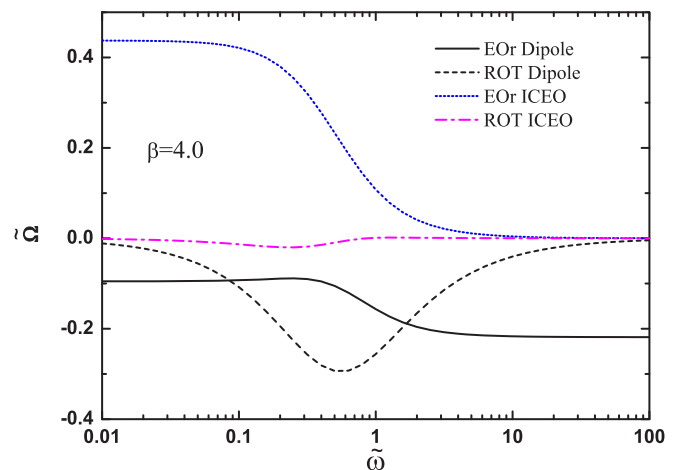


FIG. 10. Angular velocities as a function of frequency in EOr and ROT due to dipole torque and to ICEO flow for a cylinder with $\beta = 4.0$.

2.3 kHz, for KCl in water with conductivity $\sigma = 5$ mS/m, cylinder semiheight $a = 5 \mu\text{m}$, and estimating the double layer capacitance by Debye-Huckel expression $C_{\text{DL}} = \varepsilon/\lambda_D$. The maximum angular velocity in dipole torque ROT is $\Omega = 0.3\varepsilon E_0^2/\eta = 21$ rad/s for a rotating electric field with amplitude $E_0 = 10^4$ V/m. For ROT, we have implicitly assumed that the cylinder symmetry axis rotates in the plane of the applied field. In ROT experiments, it may be possible that the cylinder axis gets out of this plane because of electro-orientation tends to align the axis perpendicular to the applied field. This is beyond the scope of the present calculations. See, for instance, Ref. [32] for ROT of oblate spheroids rotating around their symmetry axis, i.e., the symmetry axis is parallel to the axis of electric field rotation.

V. CONCLUSIONS

We have studied numerically and analytically the rotation induced on uncharged metal cylinders immersed in electrolyte by AC electric fields. The induced electrical rotation of a metal nanowire in solution is originated by both the electrical torque on the induced dipole and the hydrodynamic torque on the particle due to induced charge electro-osmotic flow around the particle. For the general case, we have employed 3D numerical simulations using finite elements, while for slender cylinders we have used analytical solutions. The results of both methods are in good agreement for the slender case. The error of the analytical approximation is below 14% for the polarizability and below 4% for the ICEP angular velocity for a cylinder aspect ratio of $b/a = 0.04$. The cylinder rotation induced by the ICEO mechanism was calculated by using the Lorentz reciprocal theorem, while the rotation due to the induced dipole was calculated from the cylinder polarizability.

In EOr due to dipole torque, slender cylinders align their symmetry axis with the electric field, while short cylinders align their symmetry axis perpendicular to the field. In EOr due to ICEO flow, all cylinders align their symmetry axis with the applied field. In ROT due to dipole torque, all cylinders show counterfield rotation. In ROT due to ICEO flow, slender cylinders show cofield rotation while short cylinders show mainly counterfield rotation. For cylinders with aspect ratio close to one, the induced angular velocities are small, except for the ROT case due to dipole. For comparison, a cube only shows angular velocity different from zero for ROT due to dipole torque, which is the same behavior of metal spheres. The short cylinder with $\beta = 4$ shows alignment of its symmetry axis with the field due to ICEO flow but perpendicular orientation due to dipole torque. Since EOr due to ICEO is negligible at high frequencies, it could be possible to observe a change in orientation with frequency in experiments. Finally, the computations of the present work estimate a Λ -factor around 0.1 for the experiments given in Ref. [33].

ACKNOWLEDGMENTS

P.G.S. and A.R. acknowledge financial support from Spanish Government Ministry MEC under Contract No. FIS2014-54539P. J.E.F.M. acknowledges financial support from Secretaría de Educación Pública/PROMEP and Benemerita Uni-

versidad Autónoma de Puebla under Contracts No. 511-6/17-5295 and No. VD/702/2017, respectively.

APPENDIX A: LINEAR CHARGE ON A SLENDER CYLINDER

The applied electric field $\mathbf{E}_a = E_{0a}e^{i\omega t}\mathbf{u}_z$ induces a distribution of charges on the cylinder. Using slender-body approximation, the electric potential outside the cylinder can be written as [44–46]

$$\Phi_a = -E_{0a}z + \frac{1}{4\pi\varepsilon} \int_{-a}^a \frac{\lambda(z')}{\sqrt{(z-z')^2 + \rho^2}} dz', \quad (\text{A1})$$

where $\lambda(z)$ is an effective linear charge density placed along the cylinder axis. For an applied ac field, this induced charge $\lambda(z)$ is complex, creating in-phase and out-phase perturbed potentials. The bulk current arriving at the cylinder surface ($\rho = b$) charges the double layer capacitance, which provides an integral equation for $\lambda(z)$:

$$i\omega C_{\text{DL}}\Phi_a|_{\rho=b} = \sigma \frac{\partial \Phi_a}{\partial \rho} \Big|_{\rho=b}. \quad (\text{A2})$$

First, the radial derivative of potential at $\rho = b$ is approximated as

$$\frac{\partial \Phi_a}{\partial \rho} \Big|_b = -\frac{1}{4\pi\varepsilon} \int_{-a}^a \frac{\lambda(z')b}{((z-z')^2 + b^2)^{3/2}} dz' \approx -\frac{\lambda(z)}{2\pi\varepsilon b}, \quad (\text{A3})$$

neglecting terms of the order of $(b/a)^2$. Notice that this relation between the electric field radial component and the linear charge density is essentially the application of Gauss's law. The integral equation for $\lambda(z)$ becomes

$$4\pi\varepsilon E_{0a}z = \frac{2\lambda(z)}{i\tilde{\omega}_b} + \int_{-a}^a \frac{\lambda(z')}{\sqrt{(z-z')^2 + b^2}} dz', \quad (\text{A4})$$

where $\tilde{\omega}_b = \omega C_{\text{DL}}b/\sigma$ is a nondimensional frequency. To proceed analytically [46], the linear charge is expanded as

$$\lambda(z) \sim \frac{\lambda_1(z)}{\ln(a/b)} + \frac{\lambda_2(z)}{(\ln(a/b))^2} + \frac{\lambda_3(z)}{(\ln(a/b))^3} + \dots \quad (\text{A5})$$

Here we will expand λ up to second order.

The first order of $\lambda(z)$ is obtained by evaluating asymptotically the integral for $b \ll a$ [46],

$$\int_{-a}^a \frac{\lambda(z')}{\sqrt{(z-z')^2 + b^2}} dz' \sim 2\lambda(z) \ln(a/b), \quad (\text{A6})$$

and solving Eq. (A4). The first order of $\lambda(z)$ is [33]

$$\frac{\lambda_1(z)}{\ln(a/b)} = 2\pi\varepsilon E_{0a}z \frac{i\tilde{\omega}_b}{1 + i\tilde{\omega}_b \ln(a/b)}. \quad (\text{A7})$$

To obtain the second order, the expansion of $\lambda(z)$, with λ_1 already determined, is substituted in Eq. (A4):

$$2z = \frac{2z}{1 + i\tilde{\omega}_b \ln(a/b)} + \frac{\tilde{\lambda}_2}{i\tilde{\omega}_b [\ln(a/b)]^2} + \int_{-a}^a \frac{dz'}{\sqrt{(z-z')^2 + b^2}} \left\{ \frac{\tilde{\lambda}_1(z')}{\ln(a/b)} + \frac{\tilde{\lambda}_2(z')}{[\ln(a/b)]^2} \right\}, \quad (\text{A8})$$

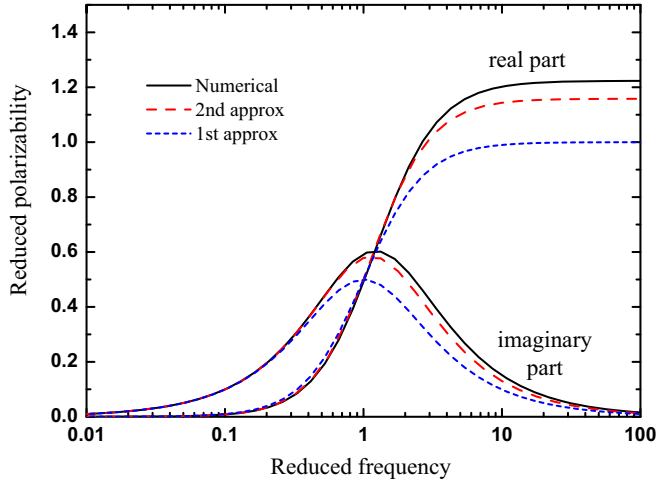


FIG. 11. Reduced polarizability $\alpha_z 3 \ln(a/b)/4\pi\epsilon a^3$ versus reduced frequency $\omega \ln(a/b)C_{DL}b/\sigma$ for $b/a = 0.0025$. The slender-body approximation is shown for the first and second order in $1/\ln(a/b)$.

where $\tilde{\lambda} = \lambda/2\pi\epsilon E_{0a}$. The integral of λ_1 is evaluated exactly and then approximated up to order $(b/a)^2$:

$$\int_{-a}^a \frac{z'}{\sqrt{(z-z')^2 + b^2}} dz' \approx -2z + z \ln \left[\frac{4(a^2 - z^2)}{b^2} \right]. \quad (\text{A9})$$

The leading approximation for the integral of λ_2 is identical to that for λ_1 , Eq. (A6). After solving for λ_2 , the linear charge up to second order is

$$\lambda(z) = \frac{2\pi\epsilon E_{0a}z}{\ln(a/b)} \Xi \left\{ 1 + \frac{1 - \ln[2\sqrt{1 - (z/a)^2}]}{\ln(a/b)} \Xi \right\}, \quad (\text{A10})$$

where $\Xi = i\tilde{\omega}_b \ln(a/b)/[1 + i\tilde{\omega}_b \ln(a/b)]$. The potential on the cylinder surface is obtained taking into account the b.c. Eq. (A2),

$$\Phi_a(b, z) = -\frac{\lambda(z)}{2\pi\epsilon i\tilde{\omega}_b} = -\frac{E_{0a}z}{1 + i\tilde{\omega}_b \ln(a/b)} \times \left\{ 1 + \frac{1 - \ln[2\sqrt{1 - (z/a)^2}]}{\ln(a/b)} \Xi \right\}. \quad (\text{A11})$$

The polarizability is the induced dipole for $E_{0a} = 1$

$$\alpha_z = \int_{-a}^a z\lambda(z)dz = \frac{4\pi\epsilon a^3}{3\ln(a/b)} \Xi \left[1 + \frac{0.947039}{\ln(a/b)} \Xi \right]. \quad (\text{A12})$$

Figure 11 compares the real and imaginary parts of the polarizability for $\beta = 0.0025$ as obtained using the slender-body approximation in the first and second order in the expansion and using finite elements. The figure depicts the reduced polarizability $\alpha_z 3 \ln(a/b)/4\pi\epsilon a^3$ versus the reduced frequency $\omega \ln(a/b)C_{DL}b/\sigma$. The convergence is slow [since it is an expansion in terms of $1/\ln(a/b)$], nonetheless, the slender approximation provides the correct trends and proper order of magnitude for the polarizability.

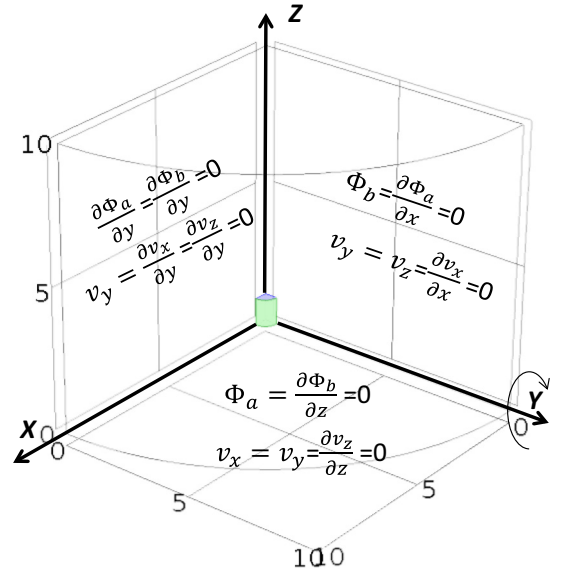


FIG. 12. Boundary conditions on planes of symmetry for electrical and hydrodynamic problems.

APPENDIX B: DETAILS OF NUMERICAL COMPUTATIONS

The symmetries of the electrical and hydrodynamic problems together with the linearity of both problems allow us to reduce the domain to an octant. Figure 12 shows the domain with the boundary conditions.

The potential Φ_a , generated by an electric field applied along the cylinder axis, is axisymmetric. It shows odd symmetry with respect to the plane $z = 0$ and even symmetry for the other two planes, $x = 0$ and $y = 0$.

The potential Φ_b , generated by an electric field applied along the X axis, shows odd symmetry with respect to the plane $x = 0$ and even symmetry for the other two planes, $y = 0$ and $z = 0$.

When the cylinder is rotating around the Y axis with angular velocity equal to one, the boundary condition on the surface of the cylinder is that the velocity is equal to $\mathbf{u}_y \times \mathbf{r}$. The velocity field generated by the rotating cylinder when its axis coincides with the Z axis has the following symmetries:

(a) The plane $y = 0$ presents even symmetry for the velocities v_x and v_z and odd symmetry for v_y . In this case, the flow at one side of the plane is a mirror image of the flow at the other side.

(b) The planes $z = 0$ and $x = 0$ present odd symmetry for the tangential velocities and even symmetry for the normal velocities. This symmetry is dictated by the fact that changing the sign of angular velocity changes the sign of the velocity field because of the linearity of equations. However, this is equivalent to rotating the system 180° around Z axis.

APPENDIX C: NONDIMENSIONAL VISCOUS COEFFICIENT

The following table shows the nondimensional viscous coefficient $\tilde{\gamma}$ for the different cylinders and the cube analyzed

β	$\tilde{\gamma}$
0.04	3.2295
0.5	18.013
1.0	48.064
4.0	1029.7
cube	60.996

in this work. It was calculated numerically as $\int [x(\mathbf{n} \cdot \mathbb{T}_2)_z - z(\mathbf{n} \cdot \mathbb{T}_2)_x] dS$, the denominator of Eq. (16). These values of the viscous coefficient are used to compute the nondimensional angular velocities as given by Eq. (33).

The value of $\tilde{\gamma}$ for $\beta = 0.04$ differs from the formula given in Ref. [52] (valid for slender rods) in less than 0.5%. This is the maximum error we estimate for the other cases.

- [1] T. B. Jones, *Electromechanics of Particles* (Cambridge University Press, Cambridge, 1995).
- [2] H. Morgan and N. G. Green, *AC Electrokintetics: Colloids and Nanoparticles* (Research Studies Press Ltd., Baldock, Hertfordshire, 2003).
- [3] R. Pethig, A. Menachery, S. Pells, and P. De Sousa, *J. Biomed. Biotechnol.* **2010**, 182581 (2010).
- [4] R. Pethig and G. H. Markx, *Trends Biotechnol.* **15**, 426 (1997).
- [5] R. J. Castellano, C. Akin, G. Giraldo, S. Kim, F. Fornasiero, and J. W. Shan, *J. Appl. Phys.* **117**, 214306 (2015).
- [6] D. Fan, F. Q. Zhu, X. Xu, R. C. Cammarata, and C. Chien, *Proc. Natl. Acad. Sci. USA* **109**, 9309 (2012).
- [7] C. Akin, J. Yi, L. C. Feldman, C. Durand, S. M. Hus, A.-P. Li, M. A. Filler, and J. W. Shan, *ACS Nano* **9**, 5405 (2015).
- [8] P. García-Sánchez and A. Ramos, *Langmuir* **33**, 8553 (2017).
- [9] C. Akin, L. C. Feldman, C. Durand, S. M. Hus, A.-P. Li, H. Y. Hui, M. A. Filler, J. Yi, and J. W. Shan, *Lab Chip* **16**, 2126 (2016).
- [10] S. Gangwal, O. J. Cayre, and O. D. Velev, *Langmuir* **24**, 13312 (2008).
- [11] S. Gangwal, A. Pawar, I. Kretschmar, and O. D. Velev, *Soft Matter* **6**, 1413 (2010).
- [12] A. M. Boymelgreen, T. Balli, T. Miloh, and G. Yossifon, *Nat. Commun.* **9**, 760 (2018).
- [13] K. D. Hermanson, S. O. Lumsdon, J. P. Williams, E. W. Kaler, and O. D. Velev, *Science* **294**, 1082 (2001).
- [14] B. Gierhart, D. Howitt, S. Chen, R. Smith, and S. Collins, *Langmuir* **23**, 12450 (2007).
- [15] P. A. Smith, C. D. Nordquist, T. N. Jackson, T. S. Mayer, B. R. Martin, J. Mbindyo, and T. E. Mallouk, *Appl. Phys. Lett.* **77**, 1399 (2000).
- [16] D. L. Fan, F. Q. Zhu, R. C. Cammarata, and C. L. Chien, *Phys. Rev. Lett.* **94**, 247208 (2005).
- [17] B. Edwards, T. S. Mayer, and R. B. Bhiladvala, *Nanoletters* **6**, 626 (2006).
- [18] P. García-Sánchez, J. J. Arcenegui, H. Morgan, and A. Ramos, *Appl. Phys. Lett.* **106**, 023110 (2015).
- [19] R. Krupke, F. Hennrich, H. v. Löhneysen, and M. M. Kappes, *Science* **301**, 344 (2003).
- [20] A. Ramos, P. García-Sánchez, and H. Morgan, *Curr. Opin. Colloid Interface Sci.* **24**, 79 (2016).
- [21] M. Z. Bazant and T. M. Squires, *Phys. Rev. Lett.* **92**, 066101 (2004).
- [22] T. M. Squires and M. Z. Bazant, *J. Fluid Mech.* **560**, 65 (2006).
- [23] V. N. Shilov and T. S. Simonova, *Colloid J. USSR* **43**, 90 (1981).
- [24] T. Miloh, *Phys. Fluids* **20**, 107105 (2008).
- [25] T. Miloh, *Phys. Fluids* **20**, 063303 (2008).
- [26] P. García-Sánchez, Y. Ren, J. J. Arcenegui, H. Morgan, and A. Ramos, *Langmuir* **28**, 13861 (2012).
- [27] P. García-Sánchez and A. Ramos, *Phys. Rev. E* **92**, 052313 (2015).
- [28] Y. Ren, D. Morganti, H. Y. Jiang, A. Ramos, and H. Morgan, *Langmuir* **27**, 2128 (2011).
- [29] J. J. Arcenegui, P. García-Sánchez, H. Morgan, and A. Ramos, *Electrophoresis* **34**, 979 (2013).
- [30] J. J. Arcenegui, P. García-Sánchez, H. Morgan, and A. Ramos, *Phys. Rev. E* **88**, 033025 (2013).
- [31] T. Miloh and B. W. Goldstein, *Phys. Fluids* **27**, 022003 (2015).
- [32] B. Weis Goldstein and T. Miloh, *Phys. Fluids* **29**, 052008 (2017).
- [33] J. J. Arcenegui, P. García-Sánchez, H. Morgan, and A. Ramos, *Phys. Rev. E* **88**, 063018 (2013).
- [34] J. J. Arcenegui, P. García-Sánchez, H. Morgan, and A. Ramos, *Phys. Rev. E* **89**, 062306 (2014).
- [35] K. A. Rose, J. A. Meier, G. M. Dougherty, and J. G. Santiago, *Phys. Rev. E* **75**, 011503 (2007).
- [36] D. Saintillan, E. Darvel, and E. Shaqfeh, *J. Fluid Mech.* **563**, 223 (2006).
- [37] A. González, A. Ramos, N. G. Green, A. Castellanos, and H. Morgan, *Phys. Rev. E* **61**, 4019 (2000).
- [38] J. Gunning, D. Y. Chan, and L. R. White, *J. Colloid Interface Sci.* **170**, 522 (1995).
- [39] V. G. Levich, *Physicochemical Hydrodynamics* (Prentice-Hall, New York, 1962).
- [40] M. Z. Bazant, M. S. Kilic, B. D. Storey, and A. Ajdari, *Adv. Colloid Interface Sci.* **152**, 48 (2009).
- [41] J. Happel and H. Brenner, *Low Reynolds Number Hydrodynamics: With Special Applications to Particulate Media*, (Springer Science & Business Media, Berlin, 2012), Vol. 1.
- [42] M. Fair and J. Anderson, *J. Colloid Interface Sci.* **127**, 388 (1989).
- [43] M. Teubner, *J. Chem. Phys.* **76**, 5564 (1982).
- [44] H. A. Stone, J. R. Lister, and M. P. Brenner, *Proc. R. Soc. London A* **455**, 329 (1999).
- [45] M. M. Hohman, M. Shin, G. Rutledge, and M. P. Brenner, *Phys. Fluids* **13**, 2201 (2001).
- [46] E. J. Hinch, *Perturbation Methods* (Cambridge University Press, Cambridge, 1991).
- [47] N. G. Loucaides and A. Ramos, *Electrophoresis* **36**, 1414 (2015).
- [48] G. Batchelor, *J. Fluid Mech.* **44**, 419 (1970).
- [49] R. Cox, *J. Fluid Mech.* **45**, 625 (1971).
- [50] Y. Solomentsev and J. L. Anderson, *J. Fluid Mech.* **279**, 197 (1994).
- [51] J. D. Jackson, *Classical Electrodynamics*, 3rd ed. (Wiley, New York, 1999).
- [52] M. M. Tirado, C. L. Martínez, and J. G. de la Torre, *J. Chem. Phys.* **81**, 2047 (1984).